

Tectonics

RESEARCH ARTICLE

10.1029/2018TC005276

Key Points:

- Variation in crustal and uppermost mantle structures within the Songpan-Ganzi terrane
- The crustal and uppermost mantle structures are correlated beneath the northeastern Songpan-Ganzi terrane and central Qilian orogen
- Tibet has evolved by crustal flow on its southeastern margin and localized mantle upwelling on its easternmost and northeastern edges

Supporting Information:

- Supporting Information S1
- Table S1

Correspondence to:

R. Zhang and Q. Wu,
 zrj@cea-igp.ac.cn;
 wuqj@cea-igp.ac.cn

Citation:

Zheng, C., Zhang, R., Wu, Q., Li, Y., Zhang, F., Shi, K., & Ding, Z. (2019). Variations in crustal and uppermost mantle structures across eastern Tibet and adjacent regions: Implications of crustal flow and asthenospheric upwelling combined for expansions of the Tibetan plateau. *Tectonics*, 38, 3167–3181. <https://doi.org/10.1029/2018TC005276>

Received 13 AUG 2018

Accepted 26 JUL 2019

Accepted article online 6 AUG 2019

Published online 24 AUG 2019

Variations in Crustal and Uppermost Mantle Structures Across Eastern Tibet and Adjacent Regions: Implications of Crustal Flow and Asthenospheric Upwelling Combined for Expansions of the Tibetan Plateau

Chen Zheng¹, Ruiqing Zhang¹ , Qingju Wu¹ , Yonghua Li¹, Fengxue Zhang¹ , Kexu Shi¹, and Zhifeng Ding¹ 

¹Institute of Geophysics, China Earthquake Administration, Beijing, China

Abstract We present new, high-resolution constraints on crustal and uppermost mantle structure of the southeastern, eastern, and northeastern Tibetan plateau and adjacent regions by combining extensive data from three regional-scale dense seismic arrays. Our results show significant differences in the crustal and uppermost mantle structure within the Songpan-Ganzi terrane. The southern part has a thick crust and high Poisson's ratio, while the crustal thickness becomes less and Poisson's ratio is nearly normal in the northeast. Prominent low-velocity anomalies appear beneath both the southern and northeastern Songpan-Ganzi terrane at depths of 20–40 km, but they are not interconnected. Seismic velocities of the uppermost mantle are slow in the northeastern Songpan-Ganzi terrane relative to the south. We further find that the crust of the central Qilian orogen is thickened but with remarkable low Poisson's ratio. Low velocities are visible in both the mid-lower crust and uppermost mantle, similar to the northeastern Songpan-Ganzi terrane. For comparison, the crustal low velocities are less pronounced beneath the central Qilian orogen. High Poisson's ratio and the mid-lower crustal anomaly of the southern Songpan-Ganzi terrane strongly indicate partial melting of the crust. Localized asthenospheric upwelling, however, can account for the coincident anomalies in both the mid-lower crust and uppermost mantle beneath the northeastern Songpan-Ganzi terrane and central Qilian orogen. We conclude that outward expansion of the Tibetan plateau has evolved by a combination of crustal flow on its southeastern margin and mantle upwelling likely induced by removal of thickened lithosphere on its easternmost and northeastern edges.

1. Introduction

Tibet, Earth's largest and highest plateau, results from the collision between the Indian and Asian continental plates since ~50–55 Ma (e.g., Van Hinsbergen et al., 2018). The present surface, particularly in central Tibet, is extremely flat, compared to the much higher relief on the southern edges of the plateau (e.g., Fielding et al., 1994). The eastern Tibetan plateau, however, exhibits a low topographic gradient and also comprises the Longmen Shan thrust belt, which has a greater topographic relief standing >5,000 m adjacent to the Sichuan basin over a short horizontal distance of ~50 km.

Several mechanical models have been proposed to explain outward enlargement of the Tibetan plateau. One of these mechanisms is distributed crustal thickening (e.g., England & Houseman, 1986) together with removal of thickened lithosphere (e.g., England & Houseman, 1989). Another general mechanism is lateral continental extrusion, which focuses mainly on the fact that the convergence between the Indian and Asian plates was oblique. The oblique convergence needs to be accommodated by extrusion along the left strike-slip faults that border Tibet's east side (e.g., Tapponnier et al., 2001). To account for the absence of significant upper crustal shortening across much of eastern Tibet during the Cenozoic, crust flow model has also been suggested (e.g., Clark & Royden, 2000). According to this model, the high topography in eastern Tibet has been sustained by lower crust flow extruded from central Tibet. The crustal flow around the Sichuan basin would have created gentle margins, while a “pile up” behind the basin might have created the narrow, steep margin. Such a flow would diverge around the Longmen Shan, one branch to the south while the other one moving north into northeastern (NE) Tibet and the Qinling orogen.

Geophysical constraints can help distinguish these competing models. Several geophysical surveys have been conducted in eastern Tibet and the adjacent regions, particularly after the Wenchuan earthquake (e.g., Bai et al., 2010; Guo et al., 2013; Liu et al., 2014; Wang et al., 2017a; Zhang et al., 2010). The majority of these studies support that the mid/lower crust west of the Longmen Shan is weak, such as low-resistivity layers at depths between 20 and 40 km (e.g., Bai et al., 2010), seismic low velocities of the mid-lower crust (e.g., Li et al., 2009; Yang et al., 2012; Yao et al., 2008), positive midcrust radial anisotropy (e.g., Li et al., 2016; Xie et al., 2013), and strong crustal attenuation (Zhao et al., 2013) in eastern and southeastern (SE) Tibet. A few of them advocate an upward expulsion of lower crustal flow that contributes to the uplift of the Longmen Shan (e.g., Lei & Zhao, 2009). Some authors believe that the crustal flow is accompanied either by strain partitioning across deep faults in eastern Tibet (Liu et al., 2014) or by mantle flow eastward through the Qinling orogen (e.g., Ye et al., 2017). However, the crustal flow model has been challenged more recently. The 3-D thermomechanical simulation indicates that the lower crust of the plateau cannot flow into the surrounding lithosphere due to its strong rheology (Chen & Gerya, 2016). A recent tomography of NE Tibet claims that the driving force for the outward growth of the Tibetan plateau is lithospheric-scale continuous deformation instead of crustal flow (Deng et al., 2018). Still, a deep reflection study argues that crustal-scale shortening is responsible for the topography development along the Longmen Shan (Guo et al., 2013).

Controversies about these models are mainly due to uncertain crustal structure and particularly poor knowledge of the underlying uppermost mantle, associated with either a shortage of data that do not provide sufficient coverage or a nonunique interpretation of separate data sets. For example, the crustal low-velocity feature under the eastern Tibet has been inferred from many studies including receiver functions, surface wave dispersion, or joint inversion of these. There is currently little consensus about its depth and spatial extent (e.g., Yang et al., 2012; Yao et al., 2008). Moreover, the correlation/uncorrelation between the crustal and upper mantle structures is crucial for interpreting lithospheric processes in the mantle. However, there are differences in existing tomographic images of the SE, eastern, and NE Tibetan plateau, particularly in uppermost mantle (e.g., Bao et al., 2015; Guo et al., 2017).

In this study, we focus on building a high-resolution seismic image of the crust and uppermost mantle across the entire eastern Tibetan plateau and surrounding regions (Figure 1). In recent years, three large-aperture dense seismic arrays have been deployed across much of the SE, eastern, and NE margin of the Tibetan plateau and their surrounding regions. By combining extensive data sets from these three seismic arrays, we constrain the crustal thickness and Poisson's ratio of our study region using receiver functions, and construct a 3-D S wave velocity (V_s) structure of the crustal and uppermost mantle by jointly inverting receiver functions and Rayleigh wave dispersions. Our study has much larger and denser station coverage than some previous studies that used the same method (e.g., Deng et al., 2018; Liu et al., 2014; Ye et al., 2017) and can thus clearly resolve the variations in crust and uppermost mantle structures across the entire eastern Tibetan plateau and surrounding regions in great detail.

2. Data and Method

2.1. Data and Receiver Functions

The stations shown in Figure 1 are from three dense seismic arrays deployed in and around eastern Tibet. Some stations represented by the blue circles are from a regional array of 288 broadband stations deployed in western Sichuan from 2007 to 2009 at intervals of 10–30 km (Liu et al., 2014). Other stations, represented by triangles and inverted triangles, are both operated by ChinArray project and are spaced ~35–40 km apart on average. They are from two large-scale arrays, one was deployed in the SE Tibet between 2011 and 2014 and the other was deployed mainly in NE Tibet from 2013 to 2016 (Wang et al., 2017a, 2017b). Each station in these arrays was equipped with a CMG-3ESPC or CMG-40 sensor and a Reftek-130 data logger.

We have obtained teleseismic waveforms recorded at ~788 stations from the three arrays, located between 26° and 38° latitude and 96° and 110° longitude. For the receiver function analysis, we select events with magnitudes larger than 5.0 at epicentral distance of 30°–90° during the recordings period of these instruments. The original horizontal components are rotated into the radial and transverse components. We compute receiver functions by deconvolving the vertical from the radial components using the iterative, time domain method of Ligorria and Ammon (1999). We use a Gaussian filter coefficient of 2.5 for the

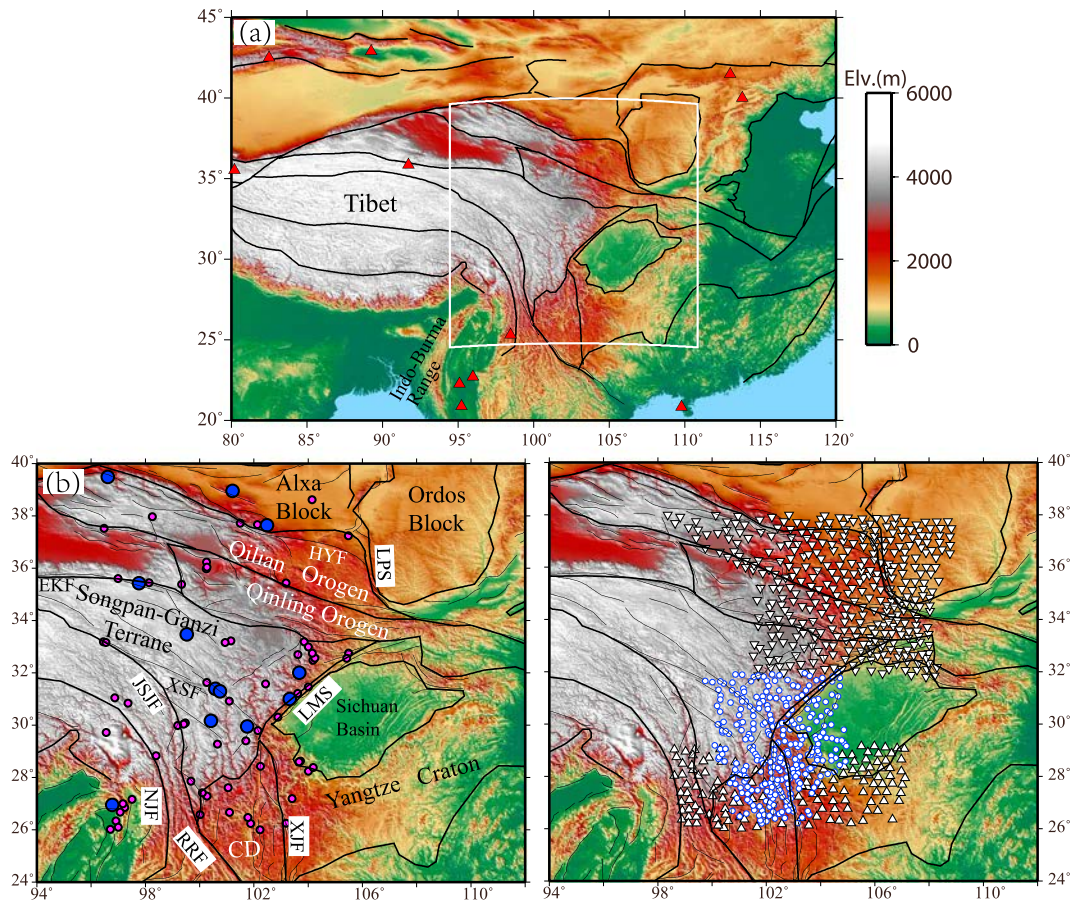


Figure 1. (a) Map showing topography in and around northeastern, eastern, and southeastern Tibetan plateau. The white region shows the location of the study area. (b) Major tectonic units and faults in our study region. Earthquakes with magnitudes of $M \geq 6.0$ (purple: $6.0 \leq M < 7.0$; blue: $M \geq 7.0$) since 1900, as taken from the United States Geological Survey catalogue, are also shown as circles. (c) Locations of portable broadband stations used in this study. Triangles and inverted triangles represent temporal stations, both operated by the ChinArray project, and blue circles are stations deployed in western Sichuan. CD = Chuan-Dian fragment; EKF = eastern Kunlun fault; HYF = Haiyuan fault; LPS = Liupan Shan; XSF = Xianshui fault; LMS = Longmen Shan; JSJF = Jinshajiang fault; NJF = Nujiang fault; RRF = Red River fault; XJF = Xiaojiang fault.

deconvolution. After the calculations, all the radial receiver functions are visually inspected to remove those with low signal-to-noise ratios.

We take the H - κ grid searching approach to measure crustal thickness and average crustal V_p/V_s ratio at each station (Zhu & Kanamori, 2000). The H - κ analysis stacks receiver functions along travel time curves of the primary P-to-S converted phase and two multiples using different crustal thicknesses (H) and V_p/V_s ratios (κ). The best estimates of H and κ are obtained when the three phases are stacked coherently. In this study, κ is varied from 1.5 to 2 at 0.001 intervals, and the weights of the primary converted phase and two multiples (2p1s and 1p2s) are assigned to 0.6, 0.3, and 0.1, respectively, in the stacking. Using the measurements of κ , we can calculate Poisson's ratio of crustal elastic properties defined as follows:

$$\sigma = 0.5 - \frac{1}{2\{(V_p/V_s)^2 - 1\}} \quad (1)$$

2.2. Joint Inversion of Receiver Functions and Rayleigh Wave Dispersions

Joint inversion of receiver functions and Rayleigh wave dispersions has been widely used to construct 3-D V_s models of crustal and uppermost mantle at high resolutions (e.g., Julià et al., 2000). Using each type of data alone suffers significant nonunique problems. Receiver functions are sensitive to velocity contrast at a boundary instead of absolute velocity structure, while surface wave dispersions are sensitive to absolute

shear velocity averages but less sensitive to velocity contrast. Thus, combining the two complimentary data sets would greatly reduce the ambiguity of inversion result from using receiver functions or dispersion data alone and can improve the vertical resolution of the depth of both crustal and uppermost mantle anomalies (e.g., Li, Song, et al., 2017; Xu et al., 2013).

We use the neighborhood algorithm (Sambridge, 1999) to jointly invert receiver function data and Rayleigh wave dispersions based on the implementation of Xu et al. (2013). We first invert a 1-D Vs model at each station and then combine them into the 3-D Vs model. In the parameterization of the 1-D model, we choose smoothed B-splines to represent velocity models. The sedimentary layer is described by two splines with three nodes, while the crust and the mantle are parameterized as cubic splines with nine fixed nodes. We adopt a uniform spline in the crust and a stretching spline for the mantle, as applied by Li, Song, et al. (2017). The Vp/Vs ratio is fixed at 2.0 and 1.795 for the sedimentary layer and the upper mantle, respectively. For the crust, we use the measured crustal Vp/Vs ratio for stations with the corresponding H- κ stacking results but fix the Vp/Vs ratio at 1.75 for stations without H- κ stacking results. A nonlinear neighborhood algorithm search is to minimize the misfit of the receiver functions and dispersions with model damping and smoothing. In our model searches, the weights for the receiver function and dispersion misfit are set at 1 and 0.25, respectively. This setting produces a \sim 60% misfit from the receiver functions and \sim 30% misfit from the dispersions in the final total residual.

Most of dispersion data in this study are obtained from local Rayleigh wave tomographic images of NE and SE Tibet (Li, Pan, et al., 2014; 2017; Pan et al., 2015). These local tomography models mainly used earthquake data recorded at the ChinArray seismic stations to produce group and phase velocity maps at periods of 10–60 s and 10–80 s, respectively. The other dispersion data are from a continent-scale Rayleigh wave tomography of China with group and phase velocities map at periods of 10–140 s (Bao et al., 2015). In our study, we extract the Rayleigh wave dispersion at periods of 10–60 s or 10–70 s for each station using linear interpolation from these tomography studies (Bao et al., 2015; Li, Pan, et al., 2014; 2017; Pan et al., 2015).

3. Results

3.1. Moho Topography and Crustal Poisson's Ratio From Receiver Functions

We check all the H- κ stacking results and the corresponding receiver function profiles. The result with larger standard deviations of H and κ , their receiver functions lacking clear Moho Ps conversions, or two multiples that both are difficult to identify, is excluded. In general, H- κ stacking works well for most of stations in our study region. But it fails at some stations located mainly along the Liupan Shan, Longmen Shan, and Xiaojiang fault, possibly due to their complex Moho structures (Figure 2c). Finally, we obtain 529 estimates of crustal thickness and Vp/Vs (Poisson's) ratio (Figure 2 and Table S1). The 1σ errors in Table S1 are calculated based on the flatness of the H- κ domain stack function at the maximum (Zhu & Kanamori, 2000).

Figure 2a shows a map of Moho topography using the H- κ stacking analysis on receiver functions. North of 27°N, the crustal thickness exhibits strong west-east variations, with a maximum of 71.8 km in the west and a minimum of \sim 30 km in the east. The west-east variation bounded by the Longmen Shan is sharp, where we find that the deeper Moho (\geq 55 km) occurs within the southern Songpan-Ganzi terrane and the Sichuan basin to the east has a shallower Moho (\leq 45 km). The Moho depth variation then became gradually as moving toward north. For example, the Moho is located \sim 45 km beneath the Ordos block, deepens gradually to \sim 50 km below the eastern Qilian orogen and reaches beyond 55 km under the central Qilian orogen. A similar gradual increase in crustal thickness from east to west also stands out within the western Qinling orogen. We also find that the crust is about 50-km thick under the northeastern Songpan-Ganzi terrane (north of 32°N), thinner than in the southern neighbor (\geq 55 km). In addition, there seems no noticeable change in Moho depth across the eastern Kunlun fault. Still, south of 26.5°N, the Moho depth decreases rapidly and is generally shallower than \sim 40 km.

The lateral variation in crustal thickness in our study region generally agree with previous receiver function studies and deep seismic sounding results, which show that the crust under the NE, eastern, and SE margins of the Tibetan plateau are significantly thicker than that under adjacent regions (e.g., He et al., 2014; Pan & Niu, 2011; Wang et al., 2010; Xu et al., 2014; Zhang et al., 2010). The crustal thickness remains almost

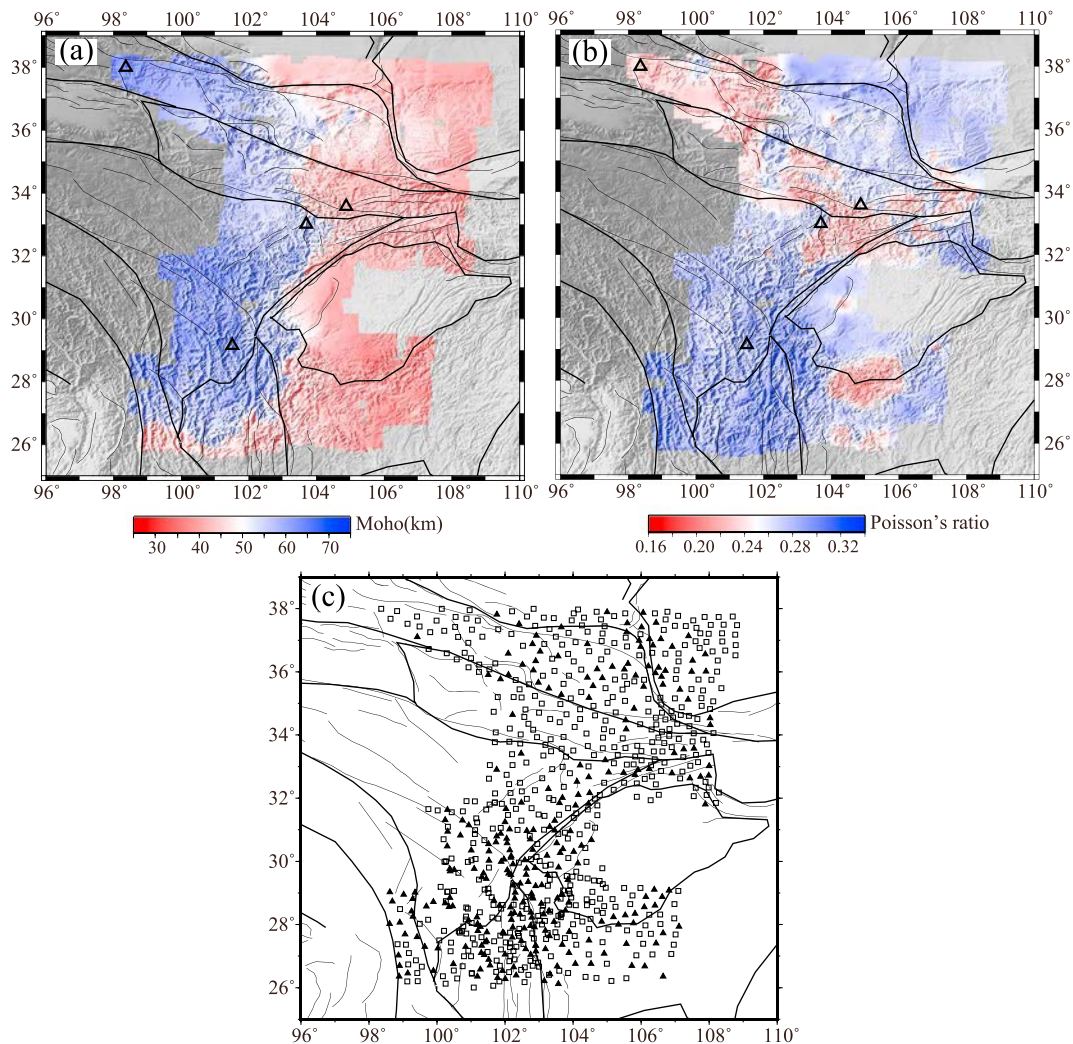


Figure 2. Map of lateral variations for (a) crustal thickness and (b) Poisson's ratio estimated from receiver functions using H- κ grid searching analysis. (c) Open squares and solid triangles represent stations with and without H- κ measurements, respectively.

unchanged beneath the western Qinling orogenic belt east of 104°E, in agreement with a flat Moho measured recently with a small linear array (Ye et al., 2017). We also note that the crust beneath the Liupan Shan at 36°N is ~50-km thick, which is slightly thinner than the estimate of 55–60 km obtained from joint inversion of receiver functions and Rayleigh wave dispersions (Guo & Chen, 2017). In addition, the steep Moho gradient at ~26.5°N coincides with the changes in both GPS velocity vectors (Shen et al., 2005) and the fast polarization directions (Chang et al., 2015) very well, which is likely related to the subduction under Indo-Burma range.

The measured Poisson's ratio of our study region varies highly between 0.17 and 0.33 with an average of 0.26 (Figure 2b). One striking feature of Figure 2b is the low Poisson's ratio ($\sigma \leq 0.24$) in the junction among the northern Longmen Shan, eastern Kunlun fault, and western Qinling orogenic belt. Poisson's ratio is also rather low beneath the central Qilian orogen, which is consistent with recent receiver function studies (Li et al., 2015; Zheng et al., 2016). In contrast, most of the Ordos block and Sichuan basin have moderate-to-high Poisson's ratio (~0.27), due to their thick sediments. More specifically, high Poisson's ratio ($0.27 < \sigma \leq 0.32$) is mainly found in the southern Songpan-Ganzi terrane, while it is nearly normal in the north (0.16–0.29 with an average of 0.25). Lateral variation in Poisson's ratios within the Songpan-Ganzi terrane has been reported by Wang et al. (2010) using data recorded by several regional networks. When

compared to that study, the pattern of variation in Poisson's ratio within this terrane is more clearly defined by our dense seismic array data.

Several examples of the H- κ stacking results and the corresponding receiver function profiles at selected stations are illustrated in Figure 3. Station X2.63039 is located in the central Qilian orogen. Its receiver functions are relatively simple and the result of H- κ grid searching shows a well-defined peak at $H = 61.4$ km and $\kappa = 1.728$ (Table S1). Stations X2.62309 and X2.51536 are located very close to each other, one in the western Qinling orogen and the other in the northeastern Songpan-Ganzi terrane. The receiver function waveforms of these two stations show similar complexities with strong signals between the Ps conversions and the first multiple phase PsPs. Station T1.KJL01 is located in the southern Songpan-Ganzi terrane and its H- κ stacking result exhibits a clear Ps conversion peak at a depth of 57.9 km, close to Moho depth of station X2.63039. The V_p/V_s ratio of station T1.KJL01 is estimated as 1.91, much higher than the value of station X2.63039.

A comparison of crustal thickness and V_p/V_s ratio between our result and the previous studies using H- κ stacking analysis (Wang et al., 2017a, 2017b) is shown in Figures S1 and S2. In the comparison, the average shift in the Moho depth is 0.03 km, and the standard deviation of the shift is 3.21 km. The shift in the average V_p/V_s ratio is 0.005 with a deviation of 0.06. Such small shifts in both the Moho depth and V_p/V_s ratio may indicate that these differences are small for the majority of the stations.

3.2. Crustal Thickness From Joint Inversion

In our joint inversion of receiver functions and dispersions, the Moho is defined as the node connecting the crustal and mantle splines and its depth can be a search parameter. The Moho topography from the joint inversion is shown in Figure 4. The first-order feature of the crustal thickness from the joint inversion is similar to that from the H- κ stacking (Figure 2a). For example, the crustal thickness exhibits systematic westward increase north of 27°N. Another similarity is the sharp south-east variation in the Moho depth around 26.5°N. However, there is a ~5-km difference between the H- κ stacking and joint inversion for the Moho depth in the northernmost region of the Songpan-Ganzi terrane.

The Moho depth from the joint inversion also depends strongly on crustal V_p/V_s ratio. In general, the crustal thickness from the joint inversion with some additional crustal V_p/V_s constraints is more compatible with the H- κ stacking results than that with fixed crustal constraints (Figures S3 and S4). The standard deviation of the Moho shifts between the results of H- κ stacking and joint inversion with some crustal V_p/V_s ratios is ~2.7 km, while the deviation is ~4.4 km with fixed values.

3.3. The 3-D V_s Structure From Joint Inversion

In addition to crustal thickness, the joint inversion result can provide a 3-D V_s structure. The V_s structure at depths of 3, 30, 50, and 90 km is presented in Figure 5 and several vertical cross-sections are shown in Figure 6.

In our study region, the V_s patterns vary dramatically from the subsurface to the uppermost mantle. At a depth of 3 km (Figure 5a), the slowest velocities are visible beneath the Ordos block and the Sichuan basin, reflecting the presence of thick sediments. High velocities can be seen in most of the Qilian orogen. This pattern is closely related to the surface geology of the study region and it changes with increasing depth. At a depth of 30 km (Figure 5b), prominent low-velocity anomalies ($V_s \leq 3.4$ km/s) appear under both the northeastern and southern Songpan-Ganzi terrane. The low-velocity anomalies in these two regions are centered mainly between depths of 20 and 40 km but are discontinuous (Figure 5b and profile GG' of Figure 6). The discontinuity is also evident from profile CC' in Figure 6, in which the crustal low-velocity anomaly thins greatly at depths that are obviously shallower than those in other profiles immediately to the south or to the north (profiles BB' and DD' in Figure 6). The crustal anomaly under the northeastern Songpan-Ganzi terrane becomes weak and disappears when it approaches the eastern Kunlun fault to the north or the Longmen Shan to the east (Figure 5b and profiles CC' and HH' in Figure 6). A less pronounced low-velocity anomaly appears under the central Qilian orogen. It is isolated and disconnected from the crustal anomalies of the northeastern Songpan-Ganzi terrane. Both the Ordos block and Sichuan basin show up with contrasting high velocities (>3.7 km/s) with a thickness of ~15–20 km in the lower crust (profiles from BB' and FF' in Figure 6). Moderate velocities are detected under both the Alxa block and the western Qinling orogen that lies between the Ordos block and Sichuan basin (Figure 5b).

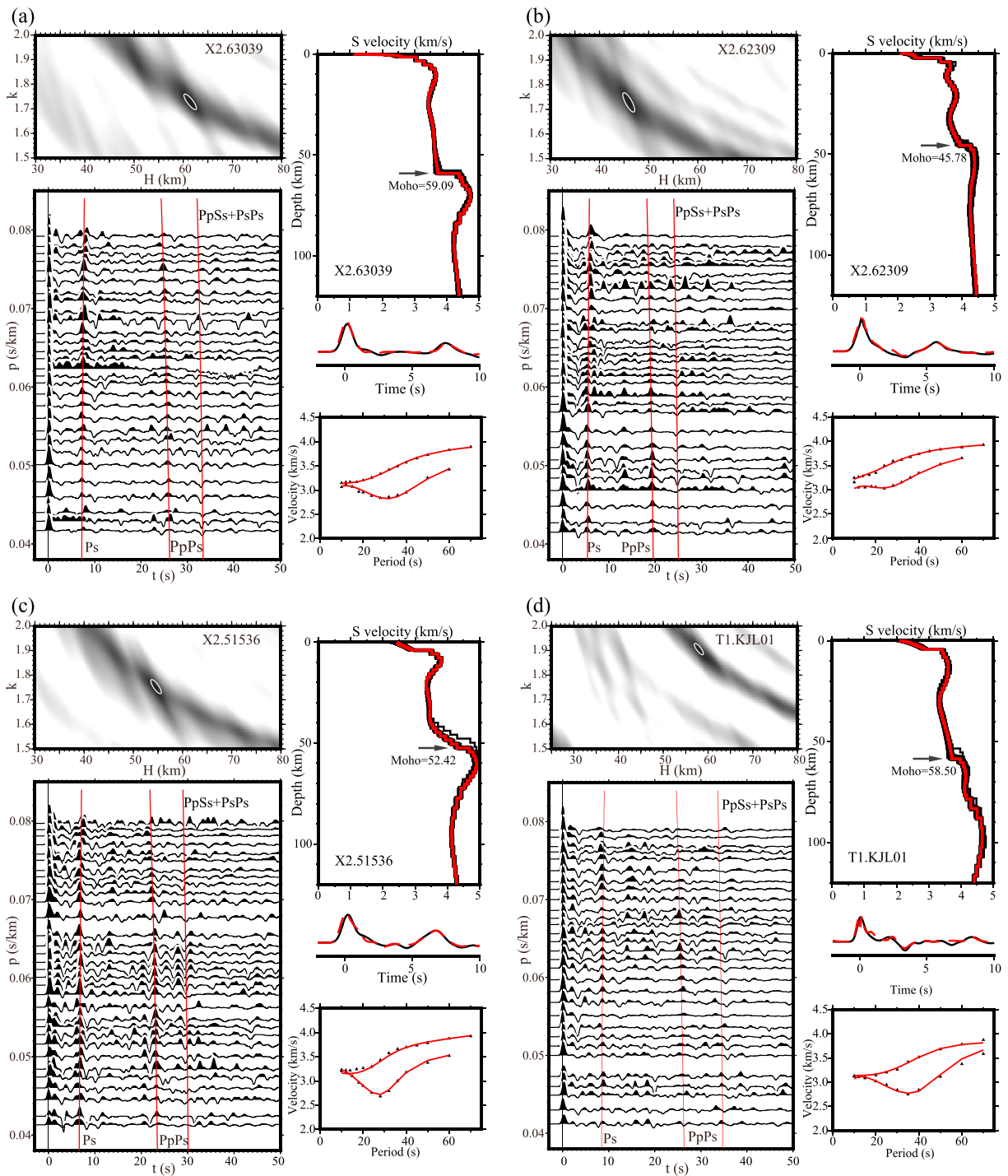


Figure 3. Examples of results of both H- κ stacking and joint inversion at stations X2.63039 (a), X2.62309 (b), X2.51536 (c), and T1.KJL01 (d). In each panel, the left frames show the H- κ analysis results and receiver function profiles with predicted travel times of the Ps, PpPs, and PpSs+PsPs by the estimated H and κ value; the 1σ uncertainties of crustal thickness and V_p/V_s ratio are given by the ellipse. The right frames show the 1-D velocity profiles from joint inversion of the receiver functions (black line shows observations and red dashed line shows prediction from the best fitting model) and surface wave dispersion curves (black triangles show observations and red curves show predictions); The best fitting model and the 200 best models in the 1-D velocity profiles are shown as red and black lines, respectively; surface wave dispersions include group velocities (low values) and phase velocities (high values). The locations of these stations are indicated in triangles in Figures 2a–2b.

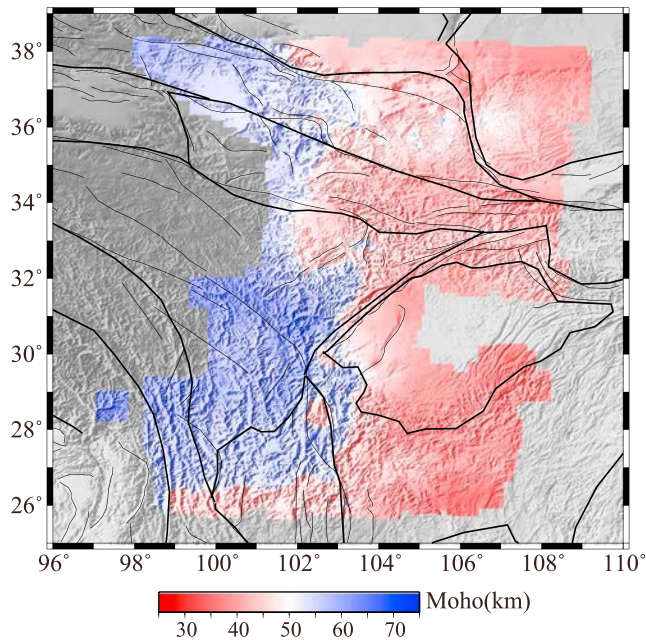


Figure 4. Map of crustal thickness map based on joint inversion of receiver functions and Rayleigh wave dispersions with some crustal V_p/V_s constraints estimated from $H-\kappa$ stacking.

At a depth of 50 km (Figure 5c), the V_s pattern corresponds very well with the lateral variation in crustal thickness. North of 27°N, the low-velocity anomalies are confined mainly west of ~103°E where the crust is generally thicker than 55 km, while the Ordos block and Sichuan basin to the east have relatively high velocities. A north-south transition from low to moderate velocities also appears around 26.5°N, similar to the pattern of variation in crustal thickness (Figure 2a). At a depth of 90 km, the V_s mainly reflect seismic velocity of the uppermost mantle. At this depth (Figure 5d), the V_s distribution changes again. Low velocities ($V_s \leq 4.3$ km/s) are identified beneath the northeastern Songpan-Ganzi terrane. Profile DD' in Figure 6 clearly shows that the uppermost mantle low velocities range from ~70 to 100 km, closely following the overlying mid-lower crustal anomaly. Slow velocities also characterize the uppermost mantle beneath the central Qilian orogen, but they are not found under the southern Songpan-Ganzi terrane (Figure 5d). In contrast, the Ordos block, central Qinling orogeny, and Sichuan basin show high velocities in the uppermost mantle.

Four examples of the joint inversion at the same stations as shown in the $H-\kappa$ stacking results are displayed in Figure 3. The 1-D velocity profiles at these stations are very different. Low velocity structures appear at ~30-km depth under stations X2.51536 and T1.KJL01. A weak low velocity in the midcrust can be still distinguished under station X2.63039. For the uppermost mantle, there are prominent low-velocity zones at 70- to 110-km depths beneath stations X2.63039 and X2.51536. The uppermost mantle

low-velocity anomaly, however, is absent under station T1.KJL01. In comparison, low velocity structures either with $V_s \leq 3.4$ km/s in mid-lower crust or with $V_s \leq 4.3$ km/s in the uppermost mantle are all very weak under station X2.62309.

3.4. Comparisons of the V_s Structure With Previous Studies

Many ambient noise tomography studies have mapped significant low-velocity anomalies at ~30-km depth within the Songpan-Ganze terrane (e.g., Jiang et al., 2014; Li, Shen, et al., 2014; Liu et al., 2014; Shen et al., 2016; Yang et al., 2012; Yao et al., 2008). The amplitude of these anomalies ($V_s < 3.45$ km/s) is comparable to the low velocities ($V_s \leq 3.4$ km/s) that we observe in the mid-lower crust of the northeastern and southern Songpan-Ganzi terrane. The crustal anomaly that gradually thins out toward the eastern Kunlun fault (Li, Shen, et al., 2014) also agrees with our observation. Some studies, however, show that the crustal low-velocity anomalies are large-scale features with spatial continuity and connectivity (Shen et al., 2016; Yang et al., 2012). This is obviously different from the disconnected features of the crustal anomalies observed between the northeastern and southern Songpan-Ganzi terrane.

Our pattern for the crustal low-velocity anomaly is also compatible with previous deep seismic sounding results, which demonstrated a low-velocity layer with thickness of ~6–8 km centered at a depth of ~20 km in the profile along 30°N (Wang et al., 2007). We do indeed observe a similar thin low-velocity anomaly at relatively shallow depths along profile CC' (Figure 6). But the extension of the crustal low-velocity layer beneath the Longmen Shan, as obtained from a deep seismic sounding study (Wang et al., 2007), differs with our observations (profiles CC' and HH' in Figure 6).

Moreover, the low velocities of the uppermost mantle observed under the northeastern Songpan-Ganzi terrane are consistent with a recent joint inversion result (Ye et al., 2017) as well as the low P_n velocity zone (Zhou & Lei, 2016). It should be noted that the uppermost mantle low velocities we image are mainly confined west of 105°E, close to the anomalous location at a depth of 75–125 km inverted from Rayleigh wave tomography (Zhang et al., 2011) but is offset from the joint inversion by Guo and Chen (2017). In the latter study, low-velocity anomaly of the uppermost mantle shifts eastward to the Liupan Shan.

We also confirm a weak low-velocity anomaly in the mid-lower crust under the central Qilian orogen (e.g., Bao et al., 2013; Jiang et al., 2014; Li, Shen, et al., 2014; Yang et al., 2012; Zheng et al., 2016). This anomaly is

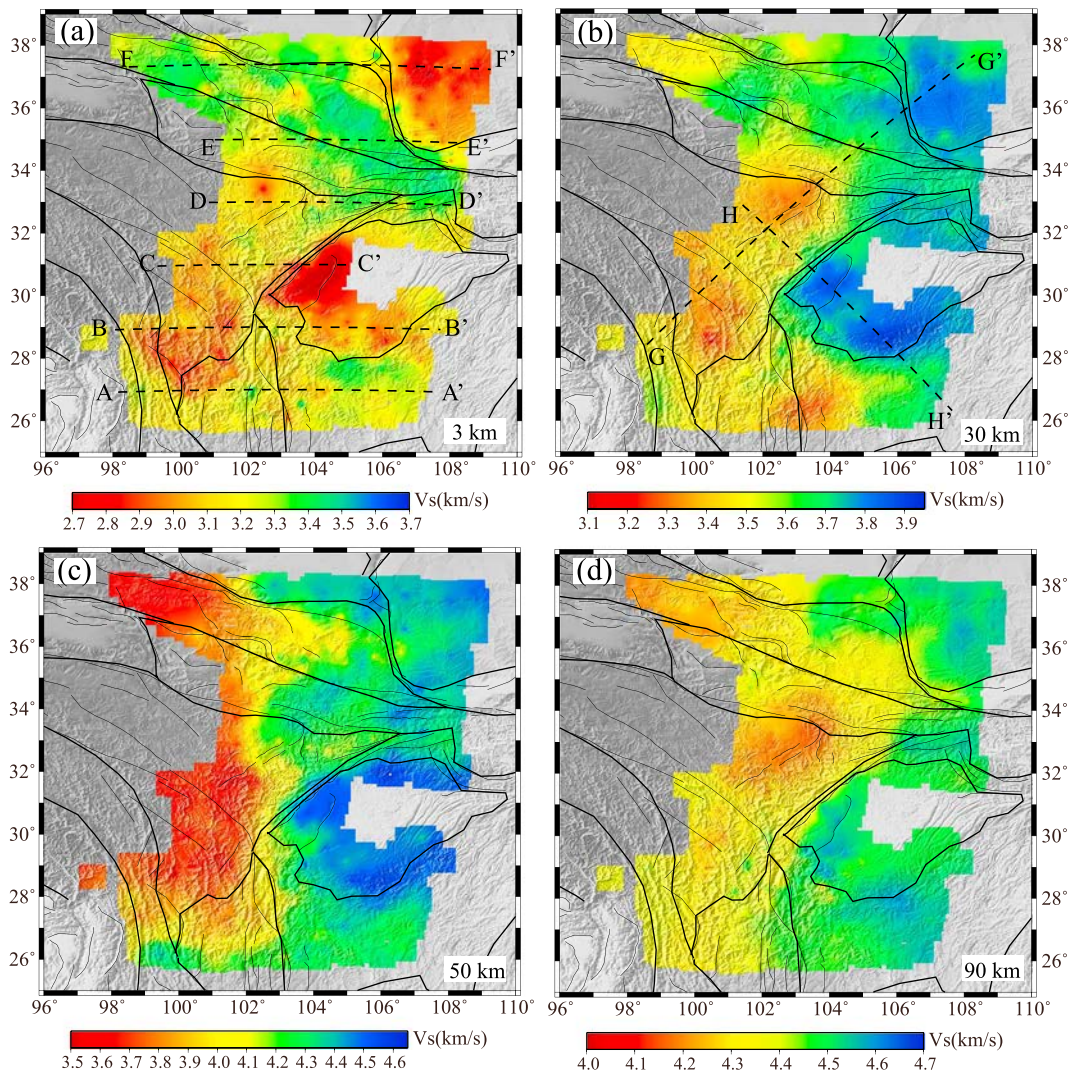


Figure 5. Shear-wave velocity at depths of (a) 3, (b) 30, (c) 50, and (d) 90 km.

directly underlain by low velocities in the uppermost mantle, similar to the pattern observed under the northeastern Songpan-Ganzi terrane. Importantly, the low velocities of the uppermost mantle beneath these two regions are clearer in the joint inversions than in the local surface wave tomography (Li, Pan, et al., 2017) and they are also not connected. This feature is different from those in some tomography studies (e.g., Bao et al., 2015; Guo et al., 2017; Li et al., 2008). For example, recent *P* wave travel time tomography study using the ChinArray stations mapped strong low velocities at ~100-km depth, stretching across the entire eastern Tibetan plateau from the Qilian and Qinling orogen belts to the Songpan-Ganzi terrane (Guo et al., 2017). The anomalous uppermost mantle structure under the Qilian orogen, however, is not apparent in previous body wave or surface wave tomography studies (e.g., Bao et al., 2015; Li et al., 2008).

4. Discussion

In general, the crustal thickness of our study region appears to have no strong correlation with the measured Poisson's ratio, the distribution of low-velocity anomalies in the mid-lower crust, or in the uppermost mantle. We find significant change in crustal thickness in west-east direction north of 27°N. Rapid north-south variation in Moho depth also appears around 26.5°N. Patterns in Poisson's ratio, the distribution of low-velocity anomalies in the crust or in the uppermost mantle, however, do not seem to be the case. This lack

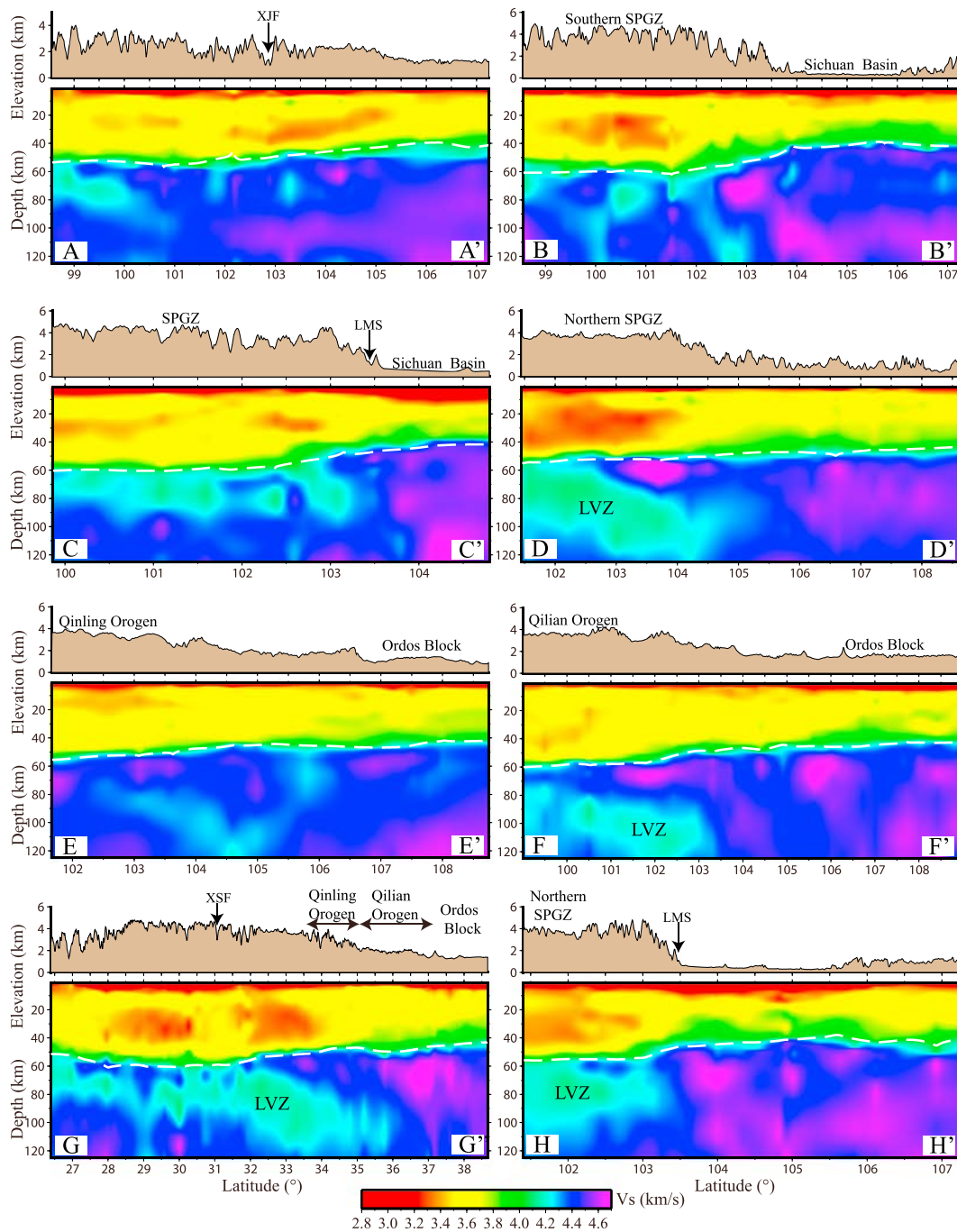


Figure 6. Cross sections of shear velocity structures along the eight profiles shown with black dashed lines in Figures 5a–5b. The topography of each profile is plotted above it. LVZ = upper mantle low-velocity zone. White dashed lines represent the Moho estimated from H- κ stacking. Note that the lateral extents of the cross sections presented between in Figure 6 are not all the same.

of significant correlation strongly indicates that crustal thickening of the Tibetan plateau on its NE, eastern, and SE margins are necessarily accommodated in very different ways.

4.1. Partial Melt of the Mid-lower Crust Beneath the Southern Songpan-Ganzi Terrane

Our findings of the thickened crust (≥ 55 km), relatively high Poisson's ratio and the low-velocity anomaly in the mid-lower crust ($V_s \leq 3.4$ km/s) under the southern Songpan-Ganzi terrane (south of 32°N) is important

for understanding the uplift of the plateau on its SE margin. Laboratory studies show that Poisson's ratio can be a good indicator of crustal composition, for example, $\sigma \approx 0.24$ for felsic granitic rock, 0.26–0.27 for intermediate rocks, and >0.28 for mafic rocks (Christensen, 1996; Zandt & Ammon, 1995). Poisson's ratio will increase significantly as the volume of the crustal melt increases (e.g., Owens & Zandt, 1997). Crustal composition can also be determined by seismic velocities. In general, mafic lower crustal rocks tend to have higher velocities than felsic ones (Christensen & Mooney, 1995). Although a mafic composition would contribute to high Poisson's ratio, it is incompatible with the low-velocity anomaly in the mid-lower crust of the southern Songpan-Ganzi terrane. Meanwhile, with a threshold value of 3.4 km/s, low-velocity anomaly in the lower crustal are usually attributed to the presence of fluid or partial melting (e.g., Liu et al., 2014; Yao et al., 2008). Therefore, we believe that relatively high Poisson's ratio with the concomitant low-velocity anomaly of the mid-lower crust is strongly suggestive of partial crustal melting beneath southern Songpan-Ganzi terrane and that the depth of the anomaly indicates that this melting occurs primarily within the mid-lower crust.

Partial melting would reflect a much weaker mid-lower crust. The mechanically weak crust is likely capable of flow and is consistent with the crust channel flow model (Clark & Royden, 2000). Our results thus support that the ductile flow within the mid-lower crust from beneath the central Tibetan plateau causes thickening and active uplift on its SE margins. The driving force for crustal flow might be due to either the release of gravitational potential energy in central Tibet (e.g., Burchfiel et al., 1995) or a traction of asthenospheric flow from below (e.g., Huang et al., 2000). Since the low-velocity anomaly of uppermost mantle under the southern Songpan-Ganzi terrane is absent, the crustal flow as a consequence of gravitational forces is preferable.

4.2. A Localized Asthenospheric Upwelling Under the Easternmost Songpan-Ganzi Terrane

The crustal and uppermost mantle structure beneath the northeastern Songpan-Ganzi terrane is quite different from the above: The crust is less thick; Poisson's ratio is nearly normal (~ 0.25), and the velocities in the mid-lower crust and uppermost mantle are both unusually low. Assuming high Poisson's ratio is an appropriate proxy for an accumulated partial melt, we suggest that such an accumulation within the mid-lower crust would not be enough to elevate the average crustal Poisson's ratio of the northeastern Songpan-Ganzi terrane, as in the southern neighbor.

The differences in crustal thickness, Poisson's ratio, and V_s structure of crust and the uppermost mantle beneath the southern and northeastern Songpan-Ganzi terrane may reflect different mechanisms of Cenozoic crustal thickening and surface uplift of the Tibetan plateau on its SE and easternmost margins. The crustal flow alone cannot explain either the variation in Poisson's ratio within the Songpan-Ganzi terrane itself or the unusually low velocities of the uppermost mantle in its northeastern part. On the other hand, the coupled low velocities in both the mid-lower crust and uppermost mantle of the northeastern Songpan-Ganzi terrane do show an apparent correlation between the crustal and uppermost mantle structure. This crust-mantle correlation favors localized asthenospheric upwelling. In such a scenario, the influx of heat from the anomalous upper mantle may play the most important role in the overlying development of the mid-lower crustal anomaly. Mantle upwelling can be a result of the subduction of slab materials. However, the anomalous uppermost mantle of the northeastern Songpan-Ganzi terrane is far from active subduction zones, such as the eastern Himalayan syntaxis (Li et al., 2008), and from the mantle upwelling imaged beneath Hainan island (e.g., Wei et al., 2012). Alternatively, the localized mantle upwelling could likely be induced by a removal of thickened lithosphere. This speculation matches previous receiver function results, which image a thinned lithosphere (70–80 km) under the northern Songpan-Ganzi terrane, compared to the lithosphere of 120- to 150-km below the Sichuan Basin (Zhang et al., 2010). To some extent, the interpretation of the localized mantle upwelling is distinguished from previous mechanisms, such as crustal flow extending to the entire lithosphere (Zhang et al., 2010) or ductile flow with a large depth range occurring down to the asthenosphere (Ye et al., 2017; Zhang et al., 2011). If so, large-scale low velocities should also have been observed in the uppermost mantle under the southern Songpan-Ganzi terrane in which the crustal flow most likely occurs. However, this is not the case except in the northeastern part.

Further north into the junction region among the northern Longmen Shan, eastern Kunlun fault, and western Qinglin orogenic belt, Poisson's ratio is rather low ($\sigma \leq 0.24$) and the prominent crustal low-velocity

anomaly is absent. This result is inconsistent with a partially molten crust and is evidence against a pile up of the lower crust that uplifts the Longmen Shan and a diversion of mid-lower crustal flow that moves north into the western Qinling orogeny.

4.3. An Initial Localized Mantle Upwelling Under the Qilian Orogen

The Qilian orogen is a fold-thrust belt that bounds the NE edge of the Tibetan plateau. It has been viewed as an important boundary condition for the formation and development of the northern parts of the Indian-Eurasia collision zone. The significant tectonic deformation of the Qilian orogen was formed during Plio-Pleistocene (Tapponnier et al., 2001). Recent magnetostratigraphy analysis studies consider that most of the crustal shortening across the Qilian orogen accumulated since the late Miocene (Wang et al., 2016), much younger than previously thought.

It is usually believed that young orogen usually has a felsic crustal composition. In the central Qilian belt, we find a thickened crust (≥ 55 km) with remarkably low Poisson's ratio (~ 0.24) and low-velocity anomalies in both the mid-lower crust and uppermost mantle. Compared to the Songpan-Ganzi terrane, the crustal low-velocity anomaly beneath the central Qilian orogen is less pronounced. As noted before, crustal Poisson's ratio is affected by both crustal composition and the degree of partial melting within the crust. The very low Poisson's ratio suggests that the crust in the central Qilian belt is predominantly felsic and that the degree of partial melting within the crust is not very significant. A predominantly felsic crustal composition accords with previous wide-angle reflection and refraction investigations (e.g., Galve et al., 2002; Liu et al., 2006).

A more felsic crustal component may have supported thickening in both the upper and lower crust. Assuming a vertically thickened lithosphere, we further speculate that the isolated crustal anomaly under the Qilian orogen is invoked mainly by a localized asthenospheric upwelling after partial removal of thickened lithosphere, thus providing a coherent explanation for the northeastern Songpan-Ganzi terrane. The very low Poisson's ratio and the less pronounced crustal anomaly of the Qilian orogen may also indicate an initiation of mantle upwelling, since this orogen represents a young and growing plateau. The mechanism we infer is different from previous studies. For example, based on the dominant felsic crustal composition, Galve et al. (2002) believed that only the upper crust is thickened in the Qinling-Qilian fold system north of the Kunlun fault. In fact, a more felsic crust does not follow the thickening of only the upper crust (Liu et al., 2006). It might also be accounted for the removal of a mafic layer from the thickened lower crust. Furthermore, Rayleigh wave tomography studies suggest that the crustal low-velocity anomaly under the northwestern Qilian Orogen has been considered an intracrustal response related to the heat produced by shortening between the North China Craton and the Tibet Plateau (e.g., Li, Shen, et al., 2014). Yet we cannot preclude the possibility of crustal heating as a result of crustal thickening. Therefore, further study is needed to resolve the crustal and particularly upper mantle structure of the Qilian orogen in more details.

4.4. Mafic Lower Crust Beneath the Ordos Block and Sichuan Basin

Both the Ordos block and the Sichuan basin have crustal moderate-to-high Poisson's ratio (~ 0.27) and are underlain by relatively high velocities in both the lower crust (3.8–4.1 km/s) and uppermost mantle (up to 4.6 km/s). Our measured Poisson's ratio is very close to the estimate based on previous receiver function studies (e.g., Pan & Niu, 2011; Wang et al., 2010). As the Poisson's ratio is less than 0.29, Pan and Niu (2011) conclude that only a small amounts of granulite-facies mafic composition at the base of the Ordos basin. Seismic refraction data reveal slower P wave (V_p) velocities in the lower crust (6.4–6.8 km/s) beneath the Ordos block, which suggests the absence of a mafic lower crust (Liu et al., 2006). Different with this seismic refraction result, we identify high velocities from the lower crust to uppermost mantle under both the Ordos block and Sichuan basin, in good agreement with previous surface-wave tomography studies (e.g., Bao et al., 2013). The high-velocity anomaly has been interpreted as a preserved old, cold, and refractory cratonic keel. Taken the average of the crustal Poisson's ratio (~ 0.27) as the value of the lower crust, the observed V_s of 3.8–4.1 km/s would correspond to the V_p of 6.76–7.3 km/s, which is consistent with a more mafic composition within the lower crust. It is notable that the calculated P wave velocity is obviously higher than those obtained from the seismic refraction data. Such difference also needs further analysis.

5. Conclusions

Extensive seismic data from the SE, eastern, and NE Tibet and its adjacent regions have been combined to investigate crustal and uppermost mantle structure that help us understand the geodynamics of eastward enlargement of the Tibetan plateau. Crustal thickness and Poisson's ratio is taken from receiver function data, while the 3-D Vs model is derived by jointly inverting of receiver functions and Rayleigh-wave dispersions.

Our result shows substantial variation in crustal and uppermost mantle structure within the Songpan-Ganzi terrane. We find thickened crust, high Poisson's ratio and prominent low-velocity anomalies at depths between 20 and 40 km under the southern part of this terrane. This combination supports that the crust in this region is partially melted and is accommodated by lateral mid-lower crust flow from beneath the central plateau. But the crustal flow does not extend to the Longmen Shan. In comparison, the northeastern Songpan-Ganzi terrane is underlain by less thickened crust, nearly normal Poisson's ratio, and anomalous low velocities in both the midcrust and uppermost mantle, which is likely resulted from localized asthenospheric upwelling. The coincident low velocities between the mid-crust and uppermost mantle also appear in the central Qilian orogen. However, unlike in the eastern Songpan-Ganzi terrane, the crust of the central Qilian orogen is thickened; Poisson's ratio is very low; the crustal anomaly is also less pronounced. These differences can be explained by an initial localized mantle upwelling driven by removal of thickened lithosphere of the Qilian Orogen. Therefore, we suggest that lateral crustal flow and mantle upwelling after removal of thickened lithosphere may both have played a key role in accommodating the uplift and expansion of the Tibetan plateau at its SE, easternmost, and NE margins. Furthermore, the Ordos block and Sichuan basin are characterized by high velocities from the lower crust to the uppermost mantle, with crustal moderate-to-high Poisson's ratio (~0.27), suggesting the preservation of an old cratonic root in these regions.

Acknowledgments

The waveform data were provided by the China Seismic Array Data Management Center at the Institute of Geophysics, China Earthquake Administration (ChinArray DMC, doi:10.12001/ChinArray.Data). The data can be found at <http://www.chinarraydmc.cn/> website. Two anonymous reviewers and the associate Editor are appreciated for their suggestions and comments that significantly improved the manuscript. L.P. Zhu is acknowledged for providing the deconvolution code. This research was supported by the NSF of China (grants 41474089, 41874073, 41474072, and 41674064) and the China National Special Fund for Earthquake Scientific Research in Public Interest (201308011).

References

- Bai, D., Unsworth, M. J., Meju, M. A., Ma, X., Teng, J., Kong, X., et al. (2010). Crustal deformation of the eastern Tibetan plateau revealed by magnetotelluric imaging. *Nature Geoscience*, 3(5), 358–362. <https://doi.org/10.1038/ngeo830>
- Bao, X., Song, X., & Li, J. (2015). High-resolution lithospheric structure beneath Mainland China from ambient noise and earthquake surface-wave tomography. *Earth and Planetary Science Letters*, 417, 132–141. <https://doi.org/10.1016/j.epsl.2015.02.024>
- Bao, X., Song, X., Xu, M., Wang, L., Sun, X., Mi, N., et al. (2013). Crust and upper mantle structure of the North China Craton and the NE Tibetan Plateau and its tectonic implications. *Earth and Planetary Science Letters*, 369, 129–137. <https://doi.org/10.1016/j.epsl.2013.03.015>
- Burchfiel, B. C., Chen, Z., Liu, Y., & Royden, L. H. (1995). Tectonics of the Longmen Shan and adjacent regions, central China. *International Geology Review*, 37(8), 661–735. <https://doi.org/10.1080/00206819509465424>
- Chang, L., Ding, Z., & Wang, C. (2015). Upper mantle anisotropy beneath the southern segment of north-south tectonic belt. *Chinese Journal of Geophysics* (Chin. Ed.), 58(11), 4052–4067.
- Chen, L., & Gerya, T. V. (2016). The role of lateral lithospheric strength heterogeneities in orogenic plateau growth: Insights from 3-D thermo-mechanical. *Journal of Geophysical Research: Solid Earth*, 121, 3118–3138. <https://doi.org/10.1002/2016JB012872>
- Christensen, N. I. (1996). Poisson's ratio and crustal seismology. *Journal of Geophysical Research*, 101(B2), 3139–3156. <https://doi.org/10.1029/95JB03446>
- Christensen, N. I., & Mooney, W. D. (1995). Seismic velocity structure and composition of the continental crust: A global view. *Journal of Geophysical Research*, 100(B6), 9761–9788. <https://doi.org/10.1029/95JB00259>
- Clark, M. K., & Royden, L. H. (2000). Topographic ooze: Building the eastern margin of Tibet by lower crustal flow. *Geology*, 28(8), 703–706. [https://doi.org/10.1130/0091-7613\(2000\)28<703:TOBTEM>2.0.CO;2](https://doi.org/10.1130/0091-7613(2000)28<703:TOBTEM>2.0.CO;2)
- Deng, Y., Li, J., Song, X. D., & Zhu, L. (2018). Joint inversion for lithospheric structures: Implications for the growth and deformation in northeastern Tibetan Plateau. *Geophysical Research Letters*, 45, 3951–3958. <https://doi.org/10.1029/2018GL077486>
- England, P., & Houseman, G. (1986). Finite strain calculations of continental deformation: 2. Comparison with the India-Asia collision zone. *Journal of Geophysical Research*, 91(B3), 3664–3676. <https://doi.org/10.1029/JB091iB03p03664>
- England, P., & Houseman, G. (1989). Extension during continental convergence, with application to the Tibetan plateau. *Journal of Geophysical Research*, 94(B12), 17,561–17,579. <https://doi.org/10.1029/JB094iB12p17561>
- Fielding, E., Isacks, B., Barazangi, M., & Duncan, C. (1994). How flat is Tibet. *Geology*, 22(2), 163–167. [https://doi.org/10.1130/0091-7613\(1994\)022<0163:HFIT>2.3.CO;2](https://doi.org/10.1130/0091-7613(1994)022<0163:HFIT>2.3.CO;2)
- Galve, A., Hirn, A., Jiang, M., Gallart, J., de Voogd, B., Lepine, J. C., et al. (2002). Modes of raising northeastern Tibet probed by explosion seismology. *Earth and Planetary Science Letters*, 203(1), 35–43. [https://doi.org/10.1016/S0012-821X\(02\)00863-4](https://doi.org/10.1016/S0012-821X(02)00863-4)
- Guo, H., Ding, Z., & Xu, X. (2017). Upper mantle structure beneath the northern South-North seismic zone from teleseismic traveltimes data. *Chinese Journal of Geophysics* (Chin. Ed.), 60(1), 86–97.
- Guo, X., Gao, R., Keller, G. R., Xu, X., Wang, H., & Li, W. (2013). Imaging the crustal structure beneath the eastern Tibetan Plateau and implications for the uplift of the Longmen Shan range. *Earth and Planetary Science Letters*, 379, 72–80. <https://doi.org/10.1016/j.epsl.2013.08.005>
- Guo, Z., & Chen, Y. J. (2017). Mountain building at northeastern boundary of Tibetan Plateau and craton reworking at Ordos block from joint inversion of ambient noise tomography and receiver functions. *Earth and Planetary Science Letters*, 463, 232–242. <https://doi.org/10.1016/j.epsl.2017.01.026>

- He, R., Shang, X., Yu, C., Zhang, H., & van der Hilst, R. D. (2014). A unified map of Moho depth and Vp/Vs ratio of continental China by receiver function analysis. *Geophysical Journal International*, *199*(3), 1910–1918. <https://doi.org/10.1093/gji/ggu365>
- Huang, W.-C., Ni, J. F., Tilmann, F., Nelson, D., Guo, J., Zhao, W., et al. (2000). Seismic Polarization Anisotropy beneath the Central Tibetan Plateau. *Journal of Geophysical Research*, *105*(B12), 27,979–27,989. <https://doi.org/10.1029/2000JB900339>
- Jiang, C., Yang, Y., & Zheng, Y. (2014). Penetration of mid-crustal low velocity zone across the Kunlun Fault in the NE Tibetan Plateau revealed by ambient noise tomography. *Earth and Planetary Science Letters*, *406*, 81–92. <https://doi.org/10.1016/j.epsl.2014.08.040>
- Julià, J., Ammon, C. J., Herrmann, R. B., & Correig, A. M. (2000). Joint inversion of receiver function and surface wave dispersion observations. *Geophysical Journal International*, *143*, 99–112.
- Lei, J., & Zhao, D. (2009). Structural heterogeneity of the Longmenshan fault zone and the mechanism of the 2008 Wenchuan earthquake (Ms 8.0). *Geochemistry, Geophysics, Geosystems*, *10*, Q10010. <https://doi.org/10.1029/2009GC002590>
- Li, C., van der Hilst, R. D., Meltzer, A. S., & Engdahl, E. R. (2008). Subduction of the Indian lithosphere beneath the Tibetan and Burma. *Earth and Planetary Science Letters*, *274*(1–2), 157–168. <https://doi.org/10.1016/j.epsl.2008.07.016>
- Li, H., Shen, Y., Huang, Z., Li, X., Gong, M., Shi, D., et al. (2014). The distribution of the mid-to-lower crustal low-velocity zone beneath the northeastern Tibetan Plateau revealed from ambient noise tomography. *Journal of Geophysical Research: Solid Earth*, *119*, 1954–1970. <https://doi.org/10.1002/2013JB010374>
- Li, H., Su, W., Wang, C., & Huang, Z. (2009). Ambient noise Rayleigh wave tomography in western Sichuan and eastern Tibet. *Earth and Planetary Science Letters*, *282*(1–4), 201–211. <https://doi.org/10.1016/j.epsl.2009.03.021>
- Li, J., Song, X., Zhu, L., & Deng, Y. (2017). Joint inversion of surface wave dispersions and receiver functions with P velocity constraints: Application to Southeastern Tibet. *Journal of Geophysical Research: Solid Earth*, *122*, 7291–7310. <https://doi.org/10.1002/2017JB014135>
- Li, L., Li, A., Murphy, M. A., & Fu, Y. (2016). Radial anisotropy beneath northeast Tibet, implications for lithosphere deformation at a restraining bend in the Kunlun fault and its vicinity. *Geochemistry, Geophysics, Geosystems*, *17*, 3674–3690. <https://doi.org/10.1002/2016GC006366>
- Li, X., Santosh, M., Cheng, S., Xu, X., & Zhong, W. (2015). Crustal structure and composition beneath the northeastern Tibetan plateau from receiver function analysis. *Physics of the Earth and Planetary Interiors*, *249*, 51–58. <https://doi.org/10.1016/j.pepi.2015.10.001>
- Li, Y., Pan, J., Wu, Q., & Ding, Z. (2014). Crustal and uppermost mantle structure of SE Tibetan plateau from Rayleigh-wave group-velocity measurements. *Earthquake Science*, *27*(4), 411–419. <https://doi.org/10.1007/s11589-014-0090-z>
- Li, Y., Pan, J., Wu, Q., & Ding, Z. (2017). Lithospheric structure beneath the northeastern Tibetan Plateau and the western Sino-Korea Craton revealed by Rayleigh wave tomography. *Geophysical Journal International*, *210*(2), 570–584. <https://doi.org/10.1093/gji/ggx181>
- Ligorria, J. P., & Ammon, C. J. (1999). Iterative deconvolution and receiver-function estimation. *Bulletin of the Seismological Society of America*, *89*, 1395–1400.
- Liu, M., Mooney, W. D., Li, S., Okaya, N., & Detweiler, S. (2006). Crustal structure of the northeastern margin of the Tibetan plateau from the Songpan-Ganzi terrane in the Ordos Basin. *Tectonophysics*, *420*(1–2), 253–266. <https://doi.org/10.1016/j.tecto.2006.01.025>
- Liu, Q., van der Hilst, R. D., Li, Y., Yao, H., Chen, J., Guo, B., et al. (2014). Eastward expansion of the Tibetan Plateau by crustal flow and strain partitioning across faults. *Nature Geoscience*, *7*(5), 361–365. <https://doi.org/10.1038/ngeo2130>
- Owens, T. J., & Zandt, G. (1997). Implications of crustal property variations for models of Tibetan plateau evolution. *Nature*, *387*(6628), 37–43. <https://doi.org/10.1038/387037a0>
- Pan, J., Li, Y., Wu, Q., & Ding, Z. (2015). Phase velocity maps of Rayleigh waves in the southern Tibetan Plateau. *Chinese Journal of Geophysics (Chin. Ed.)*, *58*(11), 3993–4006.
- Pan, S., & Niu, F. (2011). Large contrasts in crustal structure and composition between the Ordos plateau and the NE Tibetan plateau from receiver function analysis. *Earth and Planetary Science Letters*, *303*(3–4), 291–298. <https://doi.org/10.1016/j.epsl.2011.01.007>
- Sambridge, M. (1999). Geophysical inversion with a neighbourhood algorithm—I. Searching a parameter space. *Geophysical Journal International*, *138*, 479–494.
- Shen, W., Ritzwoller, M. H., Kang, D., Kim, Y., Lin, F., Ning, J., et al. (2016). A seismic reference model for the crust and uppermost mantle beneath China from surface wave dispersion. *Geophysical Journal International*, *206*(2), 954–979. <https://doi.org/10.1093/gji/ggw175>
- Shen, Z.-K., Lü, J., Wang, M., & Bürgmann, R. (2005). Contemporary crustal deformation around the southeast borderland of the Tibetan Plateau. *Journal of Geophysical Research*, *110*, B11409. <https://doi.org/10.1029/2004JB003421>
- Tapponnier, P., Xu, Z., Roger, F., Meyer, B., Arnaud, N., Wittlinger, G., & Yang, J. (2001). Oblique stepwise rise and growth of the Tibet plateau. *Science*, *294*(5547), 1671–1677. <https://doi.org/10.1126/science.105978>
- Van Hinsbergen, D. J. J., Lippert, P. C., Li, S., Huang, W., Advokaat, E. L., & Spakman, W. (2018). Reconstructing greater India: Paleogeographic, kinematic, and geodynamic perspectives. *Tectonophysics*, *760*, 69–94. <https://doi.org/10.1016/j.tecto.2018.04.006>
- Wang, C., Han, W., Wu, J., Lou, H., & Chan, W. W. (2007). Crustal structure beneath the eastern margin of the Tibetan Plateau and its tectonic implications. *Journal of Geophysical Research*, *112*, B07307. <https://doi.org/10.1029/2005JB003873>
- Wang, C., Zhu, L., Lou, H., Huang, B., Yao, Z., & Luo, X. (2010). Crustal thicknesses and Poisson's ratios in the eastern Tibetan Plateau and their tectonic implications. *Journal of Geophysical Research*, *115*, B11301. <https://doi.org/10.1029/2010JB007527>
- Wang, W., Wu, J., Fang, L., Lai, G., & Cai, Y. (2017a). Sedimentary and crustal thicknesses and Poisson's ratios for the NE Tibetan Plateau and its adjacent regions based on dense seismic arrays. *Earth and Planetary Science Letters*, *462*, 76–85. <https://doi.org/10.1016/j.epsl.2016.12.040>
- Wang, W., Wu, J., Fang, L., Lai, G., & Cai, Y. (2017b). Crustal thickness and Poisson's ratio in southwest China based on data from dense seismic arrays. *Journal of Geophysical Research: Solid Earth*, *122*, 7219–7235. <https://doi.org/10.1002/2017JB013978>
- Wang, W., Zhang, P., Pang, J., Garzzone, C., Zhang, H., Liu, C., et al. (2016). The Cenozoic growth of the Qilian Shan in the northeastern Tibetan Plateau: A sedimentary archive from the Jiuxi Basin. *Journal of Geophysical Research: Solid Earth*, *121*, 2235–2257. <https://doi.org/10.1002/2015JB012689>
- Wei, W., Xu, J., Zhao, D., & Shi, Y. (2012). East Asia mantle tomography: New insight into plate subductin and intraplated volcanism. *Asian Earth Sciences*, *60*, 88–103. <https://doi.org/10.1016/j.jseaes.2012.08.001>
- Xie, J., Ritzwoller, M. H., Shen, W., Yang, Y., Zheng, Y., & Zhou, L. (2013). Crustal radial anisotropy across Eastern Tibet and the Western Yangtze Craton. *Journal of Geophysical Research: Solid Earth*, *118*, 4226–4252. <https://doi.org/10.1002/jgrb.50296>
- Xu, T., Wu, Z., Zhang, Z., Tian, X., Deng, Y., Wu, C., & Teng, J. (2014). Crustal structure across the Kunlun fault from passive source seismic profiling in East Tibet. *Tectonophysics*, *627*, 98–107. <https://doi.org/10.1016/j.tecto.2013.11.010>
- Xu, Z., Song, X., & Zhu, L. (2013). Crustal and uppermost mantle S velocity structure under Hi-CLIMB seismic array in central Tibetan Plateau from joint inversion of surface wave dispersion and receiver function data. *Tectonophysics*, *584*, 209–220. <https://doi.org/10.1016/j.tecto.2012.08.024>

- Yang, Y., Ritzwoller, M. H., Zheng, Y., Shen, W., Levshin, A. L., & Xie, Z. (2012). A synoptic view of the distribution and connectivity of the mid-crustal low velocity zone beneath Tibet. *Journal of Geophysical Research*, *117*, B04303. <https://doi.org/10.1029/2011JB008810>
- Yao, H., Beghein, C., & van der Hilst, R. D. (2008). Surface wave array tomography in SE Tibet from ambient seismic noise and two-station analysis—II. Crustal and upper-mantle structure. *Geophysical Journal International*, *173*(1), 205–219. <https://doi.org/10.1111/j.1365-246X.2007.03696.x>
- Ye, Z., Li, J., Gao, R., Song, X., Li, Q., Li, Y., et al. (2017). Crustal and uppermost mantle structure across the Tibet-Qinling transition zone in NE Tibet: Implications for material extrusion beneath the Tibetan plateau. *Geophysical Research Letters*, *44*, 10,316–10,323. <https://doi.org/10.1002/2017GL075141>
- Zandt, G., & Ammon, C. J. (1995). Continental crust composition constrained by measurement of crustal Poisson's ratio. *Nature*, *374*(6518), 152–154. <https://doi.org/10.1038/374152a0>
- Zhang, Q., Sandovl, E., Ni, J., Yang, Y., & Chen, Y. (2011). Rayleigh wave tomography of the northeastern margin of the Tibetan plateau. *Earth and Planetary Science Letters*, *304*(1-2), 103–112. <https://doi.org/10.1016/j.epsl.2011.01.021>
- Zhang, Z., Yuan, X., Chen, Y., Tian, X., Kind, R., Li, X., & Teng, J. (2010). Seismic signature of the collision between the east Tibetan escape flow and the Sichuan Basin. *Earth and Planetary Science Letters*, *292*(3-4), 254–264. <https://doi.org/10.1016/j.epsl.2010.01.046>
- Zhao, L., Xie, X., He, J., Tian, X., & Yao, Z. (2013). Crustal flow pattern beneath the Tibetan plateau constrained by regional Lg-wave Q tomography. *Earth and Planetary Science Letters*, *383*, 113–122. <https://doi.org/10.1016/j.epsl.2013.09.038>
- Zheng, D., Li, H., Shen, Y., Tan, J., Ouyang, L., & Li, X. (2016). Crustal and upper mantle structure beneath the northeastern Tibetan Plateau from joint analysis of receiver functions and Rayleigh wave dispersions. *Geophysical Journal International*, *204*(1), 583–590. <https://doi.org/10.1093/gji/ggv469>
- Zhou, Z., & Lei, J. (2016). Pn anisotropic tomography and mantle dynamics beneath China. *Physics of the Earth and Planetary Interiors*, *257*, 193–204. <https://doi.org/10.1016/j.pepi.2016.06.005>
- Zhu, L., & Kanamori, H. (2000). Moho depth variation in southern California from teleseismic receiver functions. *Journal of Geophysical Research*, *105*(B2), 2969–2980. <https://doi.org/10.1029/1999JB900322>